




Highly excited quantum state-selective capture dynamics in slow Ar^{8+} - H_2 collisions

Md Abul Kalam Azad Siddiki ¹, G. P. Zhao ², L. Liu,^{3,*} and Deepankar Misra ^{1,†}

¹*Department of Nuclear and Atomic Physics, Tata Institute of Fundamental Research, Homi Bhabha Road, Colaba, Mumbai 400005, India*

²*College of Data Science, Jiaying University, Jiaying 314001, China*

³*Data Center for High Energy Density Physics, Institute of Applied Physics and Computational Mathematics, Beijing 100088, China*



(Received 13 October 2023; revised 19 February 2024; accepted 27 February 2024; published 25 March 2024)

We report on the combined experimental and theoretical studies of the single-electron capture collisions of Ar^{8+} projectiles with the H_2 molecules at 1, 2, and 4 keV/u collision energies. The nondissociative recoil H_2^+ molecular ions are measured in coincidence with the charge-changing Ar^{7+} projectiles. The relative cross sections of the different state-selective capture channels are obtained from the experimentally measured Q -value spectra. The $1s$ electron transfers to the highly excited $4d + 4f$, $5s$, $5p$, $5d + 5f + 5g$, $6s + 6p$, and $6d + 6f + 6g + 6h$ states are resolved experimentally. The differential scattering angle distributions for the dominant $1s$ to $5s$, $5p$, and $5d + 5f + 5g$ transitions are compared with the two-center atomic orbital close-coupling methods. A collision energy-dependent dynamical coupling effect is also observed for the $1s \rightarrow 5p_0$ and $1s \rightarrow 5p_{\pm 1}$ transitions. The dominant oscillatory structures in the scattering-angle distributions are attributed to Stueckelberg-type oscillations. In contrast, the less visible undulations in the smaller scattering angles imprint the signature of the quantum matter-wave scattering of the projectiles. The quantum nature of the oscillations in the angular distributions is further validated by classical calculations. Our study thus illustrates the highly excited quantum state-selective electron capture process and sheds light on the scattering-angle-range-dependent collision dynamics for highly charged ion-molecule collisions in the highly perturbative regime.

DOI: [10.1103/PhysRevA.109.032819](https://doi.org/10.1103/PhysRevA.109.032819)

I. INTRODUCTION

In slow, highly charged ion (HCI)-atom, -molecule, and -dimer collisions ($v < 1$ a.u., where v is the collision velocity), single or multiple electrons from the neutral targets are captured in the excited states of the projectiles [1–4]. In the electron capture process, which is the dominant process in this collision regime [5], the excited projectile states give access to the populations of the different $n\ell$ states (where n and ℓ represent the principal quantum number and orbital angular quantum number, respectively). The simple single-electron capture (SC) process allows us to study the fundamental dynamical inelastic scattering theory for different highly excited state transitions. It is also interesting to understand the fundamentals of complex collision dynamics and look for solutions to the few-body momentum exchange problem [6–8]. However, the SC process also plays an important role in the applications, i.e., diagnosis of the fusion and the astrophysical plasmas [9,10], the interaction of the highly charged solar winds with the comets [11], studies of the ioninduced radiation damage of the biological systems [12], etc.

In order to understand the state-selective capture dynamics, the angle-differential cross sections need to unfold, which imprints the collision dynamics. Also, some oscillating features are not prominent in the total cross sections, which could be visible in the differential-scattering-angle

distributions (DSADs). With the advent of cold target recoil-ion momentum spectroscopy (COLTRIMS) [13,14], it is possible to carry out the state-selective relative cross sections as well as the DSADs for a wide range of collision energies with a good resolution. In order to study the state-selective capture dynamics upon the impact of HCIs, the ground state $\text{Ar}^{8+}(2p^6)$ is one of the obvious choices because of its Ne-like close-shell electronic structure and various $n\ell$ states are well separated in energy [15] to resolve experimentally [16]. On the other hand, the adiabatic expansion of the jet allows for narrowing down the velocity distributions and the momentum resolution ($\Delta p_{\text{jet}\parallel} = m\Delta v_{\text{jet}\parallel}$) in the jet propagation direction limited by the mass of the target. This makes H_2 and He the appropriate choice to study the $n\ell$ -resolved capture dynamics using COLTRIMS. However, a few electron capture experiments for slow projectile ions (e.g., Li^+ , Na^+ , Ne^{8+}) with higher mass targets like Na and Rb have been performed using the magneto-optical trap recoil-ion momentum spectroscopy imaging technique [17–20].

In the SC process, the most probable populations of the n state are successfully predicted by the classical over-the-barrier (COB) model [21,22]. The simple scaling laws [21] for the SC process only depend on the projectile charge q and the target ionization energy I_p , and are as follows:

$$n \sim \frac{q}{\sqrt{2I_p} \frac{q+2\sqrt{q}}{1+2\sqrt{q}}}. \quad (1)$$

For Ar^{8+} -He and Ar^{8+} - H_2 SC processes, the n values are predicted around ~ 4.15 and ~ 5.10 , respectively [23]

*liu_ling@iapcm.ac.cn

†dmisra@tifr.res.in

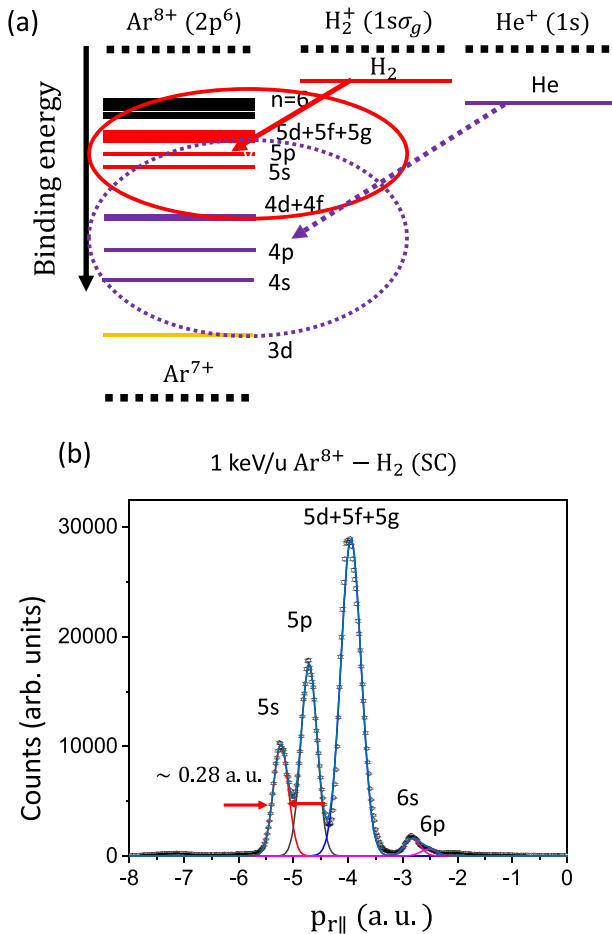


FIG. 1. (a) Schematic representation of the energy levels of the Ar^{7+} ion, the ground-state H_2 molecule, and the He atom. Dimensions are not to scale. The solid and dotted arrows indicate the dominant populations towards the $n=5$ and $n=4$ states for $\text{Ar}^{8+}\text{-H}_2$ and $\text{Ar}^{8+}\text{-He}$ SC processes, respectively. (b) The recoil longitudinal momentum distributions at the 1 keV/u collision energy.

[cf. Fig. 1(a)]. The I_p values for He and H_2 are taken as 24.6 and 16.3 eV, respectively [15,24].

A few state-selective angle-differential studies for the dominant $1s$ to $4s$, $4p$, and $4d+4f$ transitions have been reported for the $\text{Ar}^{8+}\text{-He}$ collisions at 1-6 keV/u collision energies by several groups [1,25–27]. The DSADs carry rich information about the nature of the collisions. Several quantum [19] and semiclassical [28–30] close-coupling calculations are performed in order to understand the oscillatory patterns and probe the electron-electron ($e\text{-}e$) correlation effect on the angular distributions [27]. In slow collisions, the different dynamical coupling effects on the state-selective process manifest the quasimolecular effects [25,31,32].

In the electron capture collision, the projectiles capture the electron within impact parameters b distribution, which defines the aperture radius. The scattered projectile angular distributions behave like the Fraunhofer diffraction in optics by a circular aperture. The maxima and minima in the DSADs are attributed to the matter-wave diffraction of the projectiles by the atom and are sensitive to the collision energy. van der Poel *et al.* [17] first experimentally observed the

matter-wave diffraction for the slow $\text{Li}^+\text{-Na}$ collisions. After that, it is also reported for several collision systems from low- to high-energy collisions [33–35]. Liu *et al.* [36], for the 0.1–10 keV/u $\text{He}^{2+}\text{-He}$ collisions, showed the undulations in the smaller scattering angles originated from the projectile matter-wave diffraction. In comparison, the oscillations in the higher scattering angles are attributed to the Stueckelberg-type oscillations [37–39].

In this article, we have studied the $\text{Ar}^{8+}\text{-H}_2$ SC process, which is suitable for studying the highly excited ($n=5$) quantum state-selective electron capture dynamics. The simplest H_2 molecule also provides the platform to probe the effect of $e\text{-}e$ correlation on the collision dynamics. The relative populations for the dominantly populated $n=5$ and weakly populated $n=4$ and $n=6$ states are measured experimentally. The experimental DSADs are compared with the two-center atomic orbital close-coupling (TC-AOCC) calculation [40]. The oscillations in the larger scattering angles originate from the different scattering paths, leading to identical scattering angles interfering either constructively or destructively. In comparison, the undulations in the smaller scattering angles are attributed to the projectile matter-wave diffraction. A simple mathematical model based on the optical Fraunhofer diffraction theory reproduces the diffraction fringes well. We have also shown the collision energy-dependent dynamical coupling effects for the $1s \rightarrow 5p_0$ and $1s \rightarrow 5p_{\pm 1}$ transitions (magnetic quantum number superscript 1 is used for ± 1 unless otherwise stated).

The article is organized as follows. In Sec. II we present the short descriptions of the complete experimental setup as well as the offline data analysis. In Sec. III the descriptions of the TC-AOCC method are given. The combined experimental and theoretical results and the interpretation of the angular distributions are discussed in detail in Sec. IV. Finally, in Sec. V, we summarize our major findings. In the following, atomic units are used throughout unless otherwise indicated.

II. EXPERIMENT

The experiments were performed in the electron cyclotron resonance-based ion accelerator (ECRIA) [41] facility at Tata Institute of Fundamental Research (TIFR), Mumbai, using the in-house COLTRIMS setup [26,42]. The 1, 2, and 4 keV/u Ar^{8+} projectile beam interacts perpendicularly with the supersonic H_2 jet. The supersonic jet is produced by expanding the H_2 gas of a stagnation pressure 2 bar through a 30- μm nozzle towards the source vacuum chamber. A double-stage skimmer assembly with a 400- and 750- μm diameter is used, separated by 40 mm. The distance from the nozzle to the interaction region is around 130 mm. The density of the supersonic H_2 target in the interaction region is estimated to be around $\sim 10^{11}$ molecules/ cm^3 . During the experiment, the pressure of the interaction chamber is around 7×10^{-9} mbar. The pressures of the source, skimmer, and dump chambers are 2×10^{-4} , 1.5×10^{-6} , and 8×10^{-8} mbar, respectively. All the chambers are differentially pumped. Before the interaction chamber, a cylindrical electrostatic beam cleaner is used to avoid the primary projectile beam contamination due to the beamline electron capture with residual gases. After the electron capture process, the charge-changing projectiles

are analyzed using an electrostatic charge state analyzer. The main projectile beam is deflected towards a Faraday cup, and the projectile detector consisting of a microchannel plate delay line anode (MCP + DLA) detects the other charge-changing ions. The vertical electric fields guide the recoil ions toward a similar recoil detector (MCP + DLA). Both recoil and projectile MCPs are 80 mm in diameter. We have used a two-field velocity focusing Wiley-McLaren type spectrometer [43]. The extraction, acceleration, and field-free drift region lengths are 1.5, 9.0, and 52.0 cm, respectively. The electric fields in the extraction and acceleration regions are 5.33 and 7.77 V/cm, respectively. Details can be found elsewhere [26,44]. A pair of four jaw slits are also used in the beamline to reduce the beam current in the optimal operational value. The beam current at the final Faraday cup is maintained around ~ 100 pA.

The data are stored in an event-by-event list mode using the Cobold PC software for offline analysis. For each coincidence event, the recoil detector contains the recoil ion hit positions [$X_r(i)$ and $Y_r(i)$] and time-of-flight [$T_r(i)$] information, and the projectile detector contains the charge-changing projectile hit positions [$Y_p(i)$ and $Z_r(i)$]. The three-dimensional momentum components of the recoil ions are reconstructed using the following equations,

$$p_{rx}(i) = \frac{m_r X_r(i)}{fT}, \quad (2)$$

$$p_{ry}(i) = \frac{m_r Y_r(i)}{fT} - m_r v_{\text{jet}}, \quad (3)$$

and

$$p_{rz}(i) = -Cq_r E_s \Delta T(i), \quad (4)$$

where m_r is the mass of the target recoil ion (H_2^+), T is the time-of-flight (TOF), q_r is the charge of the recoil ion, and E_s is the extraction field of the spectrometer. The bending coefficient f and the time factor C modification come from the lens used for the velocity focusing. The TOF difference between a particle with finite momentum along the spectrometer axis and zero initial momentum along the spectrometer axis is represented as $\Delta T(i) = T(i) - T_0$. v_{jet} indicates the longitudinal jet velocity along the jet propagation direction. Details can be found elsewhere [26,44].

In the electron capture collisions, the captured electrons move with the projectile. As in the laboratory frame, only the projectile has the energy source; therefore, the momentum exchanged is compensated by the relative motion between the target and the projectile. For small projectile deflection approximation and using the energy and momentum conservation, one can easily deduce the following relations of parallel ($p_{r\parallel}$), perpendicular ($p_{r\perp}$), recoil momenta and the corresponding scattering angle (θ):

$$p_{r\parallel} = -\frac{n_e v}{2} - \frac{Q}{v}, \quad (5)$$

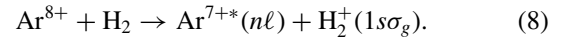
$$p_{r\perp} = p_{p\perp}, \quad (6)$$

$$\theta = \frac{p_{p\perp}}{p_{\text{ip}}}, \quad (7)$$

where $Q = (B.E)_p - (B.E)_t$, n_e , v , and p_{ip} are the binding energy differences of the captured electron between the final projectile state and the target, the number of captured electrons, the projectile velocity, and the incoming projectile momentum, respectively. From the experimental data, we have information about the $p_{r\parallel}$ and $p_{r\perp}$ for each event. We obtained the Q value and the scattering-angle distributions using the above equations.

In our experimental setup, the projectile ion moves along the x direction, the supersonic jet in the y direction, and the spectrometer field in the z direction. The $p_{r\parallel}$ and $p_{r\perp}$ momenta can be calculated from the recoil p_{rx} and $\sqrt{p_{ry}^2 + p_{rz}^2}$, respectively. In the 1 keV/u Ar^{8+} - H_2 SC process, the longitudinal recoil resolution ($\Delta p_{r\parallel}$) is estimated to be around 0.28 ± 0.03 a.u. for the $1s \rightarrow 5s$ transition [cf. Fig. 1(b)]. In the present 1–4 keV/u Ar^{8+} - H_2 collision system, $1s \rightarrow 5s$ and $1s \rightarrow 5p$ transitions are resolved experimentally and are separated by $\simeq 3.1$ eV [15]. On the other hand, the separations between the $5d$ - $5f$ and $5f$ - $5g$ states are $\simeq 1.24$ and 0.1 eV [15], respectively. Therefore, the thick horizontal line in Fig. 1(a) donates states that are not experimentally resolved. The $\Delta p_{r\parallel}$ is estimated around 0.37 ± 0.03 a.u. for the mixed $5d + 5f + 5g$ states.

In the SC process, the different $n\ell$ -resolved excited states of the Ar^{7+} projectiles are calculated using the ground-state $\text{Ar}^{8+}(2p^6)$ ions with the electronic ground state of the $\text{H}_2^+(1s\sigma_g)$ ions and are given by



The contamination from the metastable $\text{Ar}^{8+}(2p^5 3s)$ ions extracted from the ECRIS is negligible [45]. Also, the large inelasticity (Q value) in the SC process results in the loss of the corresponding H_2^+ ions from the spectrometer as the applied fields are small.

III. THEORY

The TC-AOCC method for dealing with heavy-particle collisions is described in detail in Refs. [6,40]. This method expands the total scattering wave function in terms of the single-center electronic states centered on the target and the projectile, respectively. The coupled equations for the state amplitudes are produced after inserting the total wave function into the time-dependent Schrödinger equation. The atomic states of the projectile (A) and the target (B) are determined by diagonalization of the Hamiltonian of the projectile (and the target) over the even-tempered basis:

$$\phi_{nlm}(\vec{r}) = \sum_k c_{nk} \chi_{klm}(\vec{r}). \quad (9)$$

It should be noted that a single-center approximation has been used for the hydrogen molecular target, and the H_2 target is treated as an atom in the present calculations. The atomic states of H_2 have also been obtained by Eq. (9).

The approximate straight-line motion is employed for the nuclear motion $\vec{R}(t) = \vec{b} + \vec{v}t$ (where b represents the impact parameter and v represents the collision velocity). In order to derive the TC-AOCC equations, the total electron wave function ψ is expanded in terms of the single-center electronic

states of the two centers (ϕ_A and ϕ_B):

$$\Psi(\vec{r}, t) = \sum_i a_i(t) \phi_i^A(\vec{r}, t) f^A(r, t, v) + \sum_j b_j(t) \phi_j^B(\vec{r}, t) f^B(r, t, v), \quad (10)$$

where f^A and f^B represent the translational factors of the plane-wave electron. Inserting Eq. (10) into the time-dependent Schrödinger equation yields

$$\left(H - i \frac{\partial}{\partial t} \right) \Psi = 0, \quad (11)$$

with the electronic Hamiltonian

$$H = -\frac{1}{2} \nabla_r^2 + V_A(r_A) + V_B(r_B), \quad (12)$$

where $V_A(r_A)$ and $V_B(r_B)$ represent the electron interaction with the projectile core (Ar^{8+}) and the target core (H_2^+), respectively.

The model potentials from Refs. [16,46] are used for V_A and V_B as follows:

$$V_A(r) = -\frac{8}{r} - \frac{10}{r} \exp(-5.50r) - 5.50 \exp(-5.50r), \quad (13)$$

and

$$V_B(r) = -\frac{1}{r} - \frac{1}{r} \exp(-2.697r) - 0.6535 \exp(-2.697r). \quad (14)$$

For the H_2 target, the above model potential can produce an accurate ionization energy of H_2 . Then, the first-order coupled differential equations for the amplitudes $a_i(t)$ and $b_j(t)$ can be obtained as

$$i(\dot{A} + S\dot{B}) = HA + KB, \quad (15)$$

$$i(\dot{B} + S^+\dot{A}) = \bar{K}A + \bar{H}B, \quad (16)$$

where the vectors A and B represent the amplitudes a_i ($i = 1, 2, \dots, N_A$) and b_j ($j = 1, 2, \dots, N_B$), respectively. S is the overlap matrix, and its transposed form is denoted as S^+ . H and \bar{H} represent the direct coupling matrices, while K and \bar{K} are the electron exchange matrices. The solutions to Eqs. (15) and (16) are obtained with the initial conditions

$$a_i(-\infty) = \delta_{1i}, \quad b_j(-\infty) = 0. \quad (17)$$

By integrating the transition probabilities over the impact parameter b , the partial cross sections for the charge-exchange process can be obtained as

$$\sigma_{\text{exc},l} = 2\pi \int_0^\infty |a_i(+\infty)|^2 b db. \quad (18)$$

The angle-differential cross sections for the $i \rightarrow j$ transition can be obtained by

$$\frac{d\sigma_{ij}}{d\theta} = 2\pi \sin \theta |A_{ji}|^2, \quad (19)$$

where the scattering amplitudes A_{ji} determined by the impact-parameter-dependent transitions amplitudes are given by

$$A_{ji}(\theta) = \gamma \int_0^{+\infty} b F(b) J_{|m_j - m_i|} \left[2b\mu v \sin \frac{\theta}{2} \right] db, \quad (20)$$

where

$$F(b) = a_{ji} e^{2(i/v)Z_T Z_P l n b}, \quad (21)$$

$\gamma = \mu v (-i)^{|m_j - m_i| + 1}$, μ is the reduced mass of the projectile and the target, and m_j (m_i) represents the magnetic quantum number of the final (initial) state. The function J represents the Bessel function of the first kind. For a given impact parameter b , the transition amplitude a_{ji} is calculated from Eqs. (15) and (16). The term $e^{2(i/v)Z_T Z_P l n b}$ denotes the eikonal phase due to the Coulomb repulsion between the target and the projectile nuclei, and Z_T and Z_P are the corresponding effective charge.

IV. RESULTS AND DISCUSSION

A. $n\ell$ -resolved relative cross sections

In the Ar^{8+} - H_2 single-electron capture collisions, the most probable distributions for the $n = 5$ state are observed experimentally, which is also predicted by the COB model [see Eq. (1)]. More than 90% of populations are distributed in the $n = 5$ state and the other small contributions are for the $n = 6$ and $n = 4$ states. As collision energies increase from 1 to 4 keV/u, the spectrum also broadens, and the contributions of the $n = 6$ and $n = 4$ states start to increase slowly. This is in accordance with the broadening of the reaction window with $v^{0.5}$ estimated using the extended classical over-the-barrier model [22]. The orbital quantum numbers (ℓ), i.e., ℓ -selective contributions, are also identified. We have identified the final $n\ell$ -resolved contributions in the Q -value spectra which assigned the Ar^{7+*} states as follows: $6d + 6f + 6g + 6h$, $6s + 6p$, $5d + 5f + 5g$, $5p$, $5s$, and $4d + 4f$ (cf. Fig. 2). As the distributions are convoluted with the supersonic jet profile, which is Gaussian, we fit the Q -value distributions using multi-peak Gaussian fitting. The $5d + 5f + 5g$ state is the most populated state within this collision regime. The relative population of the above-identified states is tabulated in Table I. It can be seen that the TC-AOCC calculation slightly underestimates the populations of the dominant $n = 5$ and 6 states (most cases) and much overestimates the $4d + 4f$ states. The capture radii or impact parameters b are needed to be smaller to populate the $4d + 4f$ states due to their higher inelasticity (Q value). Therefore, the TC-AOCC calculations overestimate the populations for the small- b -induced collisions.

B. Angular distributions

In order to get an insight into collision dynamics for the different state-selective transitions, the DSADs imprint the ongoing collision processes. Figure 3 shows the two-dimensional momentum density distributions in the (a) 1, (b) 2, and (c) 4 keV/u Ar^{8+} - H_2 SC processes. It can be seen that the recoil transverse momentum is higher at 1 keV/u collision energy and decreases as collision energies increase to 4 keV/u. This can be understood at slow collisions, where the interaction time is higher (around $\sim 1 \times 10^{-15}$ s at 1 keV/u collision energy for an interaction distance of ~ 8 a.u.), and the electronic cloud can be adiabatically adapted to the small internuclear separation. The dominant $5s$, $5p$, and $5d + 5f + 5g$ states imprint oscillating lobes in their transverse momentum profiles and strongly depend on the collision energy. One thing is observed: the mean transverse momentum value for the

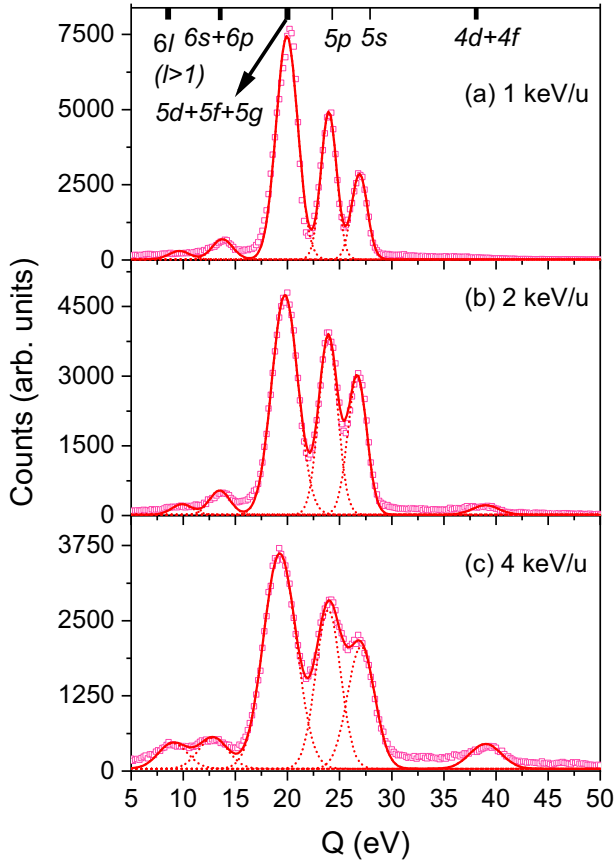


FIG. 2. Q -value spectra for the $\text{Ar}^{8+}\text{-H}_2$ SC process at 1, 2, and 4 keV/u collision energies. The red dotted lines indicate the Gaussian fitting curves and the red solid lines are the sums of all Gaussian fittings.

weak $1s \rightarrow 4d + 4f$ transition stays higher than the values of the other transitions. The $4d + 4f$ state is mostly populated at smaller internuclear separation as the inelasticity (Q value) is higher.

Figure 4 compares DSADs for the experiment and the theory for the $1s \rightarrow 5s$, $1s \rightarrow 5p$, and $1s \rightarrow 5d + 5f + 5g$ transitions in the 1, 2, and 4 keV/u $\text{Ar}^{8+}\text{-H}_2$ SC processes. The TC-AOCC calculations reproduced the oscillations in the DSADs visible in the experimental data. The origin of these oscillations can be understood from the transition amplitudes obtained from Eq. (21). The state-selective scattering amplitudes are the coherent sum of the eikonal phases accumulated during the projectile-target relative motions. The individual paths are defined by the impact parameter b , which corresponds to a definite scattering angle. The different impact parameters b result in similar scattering angles that could interfere constructively or destructively, leading to coherent oscillations in scattering-angle distributions. This kind of oscillation is known as the Stueckelberg oscillation, which was previously reported for slow ion-atom collisions [37–39].

It can be noted that at 1 keV/u collision energy, the mean of the dominant oscillatory lobes obtained from the TC-AOCC method is shifted around ~ 1.36 , 1.33 , and 1.27 times with respect to the experimentally measured dominant oscillatory lobes for the $1s$ to $5s$, $5p$, and $5d + 5f + 5g$ transitions, re-

TABLE I. Relative cross sections (in %) of the different final projectile states of $\text{Ar}^{7+}(n\ell)$ in the $\text{Ar}^{8+}\text{-H}_2$ SC process at 1, 2, and 4 keV/u collision energies. The statistical errors are less than $\sim 0.15\%$ for the dominant $n = 5$ state and $\sim 0.6\%$ for the weak $n = 4$ and 6 states.

Collision energy E (keV/u)	Final projectile $n\ell$ state $\text{Ar}^{7+}(n\ell)$	Relative cross section (Experiment)	Relative cross section (TC-AOCC)
1	$6d + 6f + 6g + 6h$	1.1	1.0
	$6s + 6p$	3.9	2.1
	$5d + 5f + 5g$	52.4	46.9
	$5p$	26.5	25.8
	$5s$	15.1	16.4
	$4d + 4f$	1.0	7.1
2	$6d + 6f + 6g + 6h$	1.7	1.5
	$6s + 6p$	4.1	2.5
	$5d + 5f + 5g$	45.0	40.2
	$5p$	26.9	23.7
	$5s$	20.5	19.1
4	$4d + 4f$	1.8	11.3
	$6d + 6f + 6g + 6h$	4.1	4.5
	$6s + 6p$	5.2	3.0
	$5d + 5f + 5g$	42.4	35.7
	$5p$	25.7	21.6
	$5s$	18.9	17.6
	$4d + 4f$	3.7	14.1

spectively [cf. Fig. 4(a), 4(b), and 4(c)]. One of the possible reasons is that in the TC-AOCC calculations, the e - e interaction term is excluded for the single-center and single-active electron H_2 molecules (see Sec. III). Recent studies [27] based on the two-active electrons show a good agreement with the experiment. The electronic Hamiltonian (H_{TA}) [29] for two-active electrons can be expressed as follows:

$$H_{\text{TA}} = \sum_{i=1,2} \left[-\frac{1}{2} \nabla_i^2 + V_T(r_i) + V_P(r_i^p) \right] + \frac{1}{|\vec{r}_1 - \vec{r}_2|}, \quad (22)$$

where \vec{r}_i and $\vec{r}_i^p = r_i - \vec{R}(t)$ are the position vectors of the electrons with respect to the target and the projectile, respectively.

The electronic Hamiltonian [see Eq. (12)] of the TC-AOCC calculation contains the electron-projectile and the electron-target interactions. Both are attractive interactions in nature. On the other hand, the inclusion of the e - e correlation is added as a positive interaction term in the electronic Hamiltonian. Therefore, without the e - e correlation in Eq. (12), the higher attractive interactions result in relatively close collisions and correspondingly result in relatively higher scattering angles. It is also observed that the third oscillatory lobe in the higher scattering angles (≥ 0.6 mrad) in the 1 keV/u $1s \rightarrow 5s$ transition is suppressed in the experiment. Quantitatively, this oscillatory lobe at higher scattering angles originates from the smaller impact parameters b , i.e., close collisions. This implies that in close collisions, complex molecular mechanisms mostly govern the electronic dynamics where electron capture occurs between the different molecular states through the curve crossing. The discrepancies between the TC-AOCC

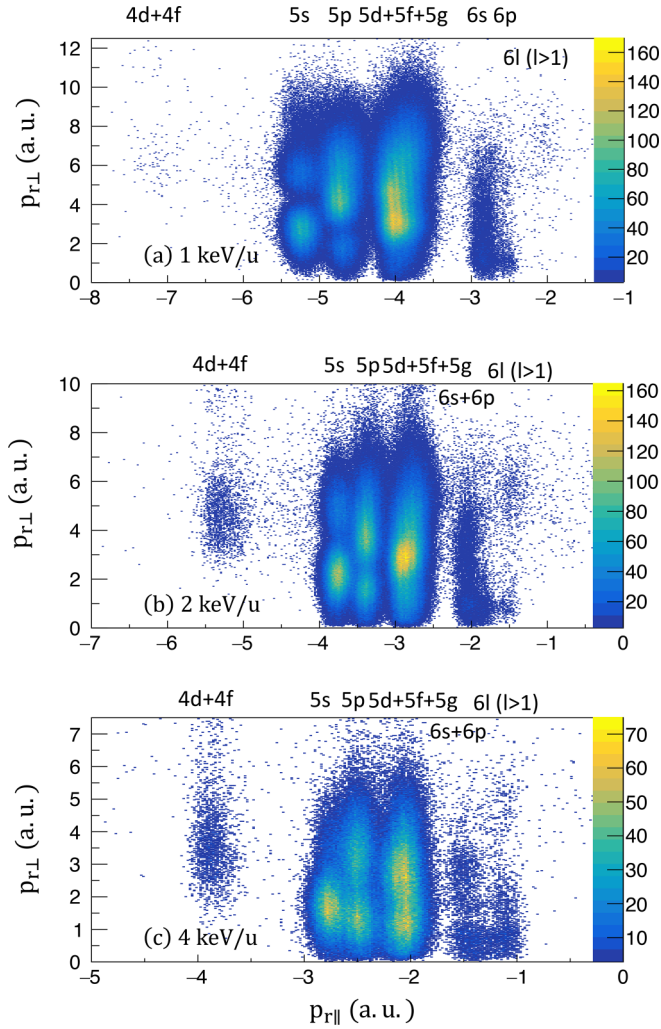


FIG. 3. Two-dimensional momentum density plots for the (a) 1, (b) 2, and (c) 4 keV/u Ar^{8+} - H_2 SC processes. The horizontal and vertical axes represent the recoil longitudinal and transverse momenta, respectively in a.u. The color bar on the right side represents the counts in arbitrary units.

calculations and the experiments for the $1s \rightarrow 5s$, $1s \rightarrow 5p$, and $1s \rightarrow 5d + 5f + 5g$ transitions have been observed at the larger scattering angles, i.e., the close collisions. The absence of e - e correlation in the electronic Hamiltonian of the single-center and single-active electron approximations for the H_2 molecule influences the dynamics. The Ar^{8+} - H_2 collision system is a three-center Coulomb problem where the molecular orientation is expected to influence the state-selective partial cross sections and the respective collision dynamics. However, the Ar^{8+} projectile sees an effective single-electronic cloud due to the large single-electron capture radius (~ 11.7 a.u. according to COB model) compared to the H_2 bond length (1.4 a.u.). Therefore, one can expect less molecular-orientation-dependent effects. Hence, the TC-AOCC calculations qualitatively reproduced the nature of the oscillating structures in the DSADs.

It can be seen that for the $1s \rightarrow 5p$ transition, the intensity of the second oscillatory lobe is suppressed as the collision energy increases from 2 to 4 keV/u. This indicates the

large- b -induced collisions (i.e., soft collisions) start to dominate as collision energy increases and corresponding quasimolecular effects (i.e., electronic dynamics governed by the molecular mechanisms) decrease with decreasing the interaction time. This behavior is clearly reflected in the state-selective transverse momentum distributions (cf. Fig. 3). According to the classical Rutherford scattering theory, the scattering angle is inversely proportional to the product of the collision energy and the impact parameter b [6]. A similar behavior has been observed for the $1s \rightarrow 5d + 5f + 5g$ transition.

In the quasimolecular picture, in slow collisions, the electronic cloud can be adapted to the small internuclear separation between the slow-moving nuclei. The electronic transitions in the small impact parameter b occur through the curve crossing between the different molecular states [47]. With increasing collision energy, the quasimolecular effects are expected to decrease, i.e., the small- b -induced collisions decrease. Also, the presence of the e - e interaction is expected to influence the collision dynamics. As our TC-AOCC calculations approximated the single-center and single-active H_2 targets, the effect of the e - e interaction would be reflected in the magnetic subshell selective DSADs. To gain insight into the different dynamical coupling effects in the Ar^{8+} - H_2 collision system, we discuss the DSADs for the $1s \rightarrow 5p_0$ and $1s \rightarrow 5p_1$ transitions in Sec. IV B 1.

1. Dynamical coupling effects

In our collision range, v is much smaller ($v \sim 0.28$ a.u. at 2 keV/u) than the orbital electron velocity of the H_2 molecule. During the collision, it forms an $(\text{ArH}_2)^{8+}$ quasimolecular ion where the electronic cloud is adiabatically adapted into the slow-moving nuclei. As a result, different dynamical coupling effects arise [6,25,48].

In the xz scattering plane, the time-dependent operator ($\frac{\partial}{\partial t}$) can be expressed as [6]

$$\frac{\partial}{\partial t} = v_R \frac{\partial}{\partial R} + \frac{vb}{R^2} iL_y, \quad (23)$$

where v_R represents the radial velocity and L_y represents the projection of the angular momentum perpendicular to the collision plane xz .

Between the χ_k and χ_m states, the dynamical coupling can be written as

$$\langle \chi_k | \frac{\partial}{\partial t} | \chi_m \rangle = v_R \langle \chi_k | \frac{\partial}{\partial R} | \chi_m \rangle + \frac{vb}{R^2} \langle \chi_k | iL_y | \chi_m \rangle, \quad (24)$$

where the terms $\langle \chi_k | \frac{\partial}{\partial R} | \chi_m \rangle$ and $\langle \chi_k | iL_y | \chi_m \rangle$ represent the radial coupling and the rotational coupling, respectively.

The radial coupling operator $\frac{\partial}{\partial R}$ couples the states that have the same projection of the angular momentum on the internuclear axis, i.e., $\Delta m_{fi} = 0$. The rotational coupling operator iL_y couples the states with $\Delta m_{fi} = \pm 1$. Quantitatively, the rotational coupling arises from the rotation of the internuclear axis between the target and the projectile. During the collision, the internuclear axis rotates with respect to the space-fixed frame, resulting in a symmetry change. On the other hand, the radial coupling arises from the inertia to keep the orbitals fixed in space.

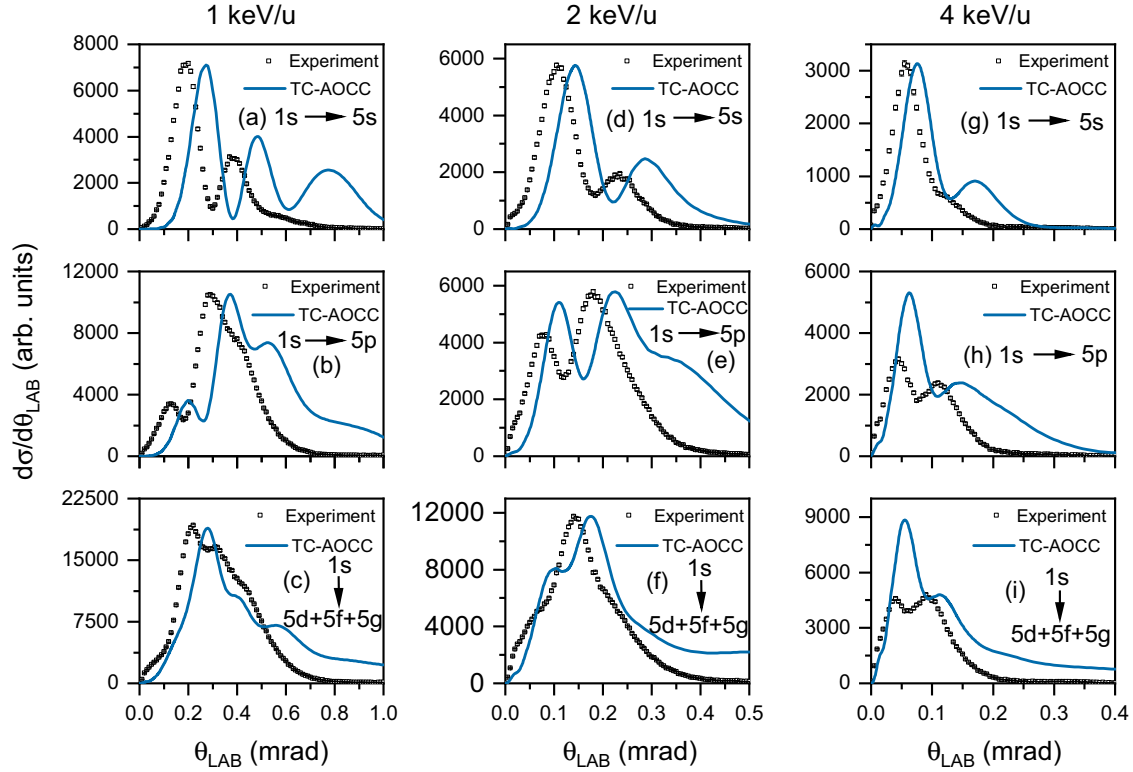


FIG. 4. DSADs of the state-selective electron capture for the $1s$ to $5s$, $5p$, and $5d + 5f + 5g$ states for 1 keV/u (left panels), 2 keV/u (middle panels), and 4 keV/u (right panels) Ar^{8+} - H_2 collisions. The black solid symbols represent the experimental data, and the blue lines represent the TC-AOCC calculations. The TC-AOCC data are normalized with respect to the experimental counts.

Figure 5 shows the DSADs for the $1s \rightarrow 5p_0$ and $1s \rightarrow 5p_1$ transitions at (a) 2 and (b) 4 keV/u collision energies are obtained from the TC-AOCC method. The modulations in the DSADs for the $5p_0$ and $5p_1$ states are in different phases with respect to each other. This is the result of the oscillating nature of the electronic transitions accumulated with the eikonal phase $F(b)$ [see. Eq. (21)].

The relative population of the $5p_0$ and $5p_1$ states are tabulated in Table II. At 2 keV/u collision energy, the $5p_1$ state dominates over the $5p_0$ state. It implies the strong alignment of the $5p_1$ state with respect to the internuclear axis. As collision energy increases to 4 keV/u, the $5p_1$ state still has the dominant contribution, but the relative contribution between $5p_1$ and $5p_0$ states decreases. It has been seen that the radial coupling mostly occurs at the large internuclear separation where the avoided crossing between the two states takes place. In the other way, rotational coupling occurs at the smaller internuclear separation [19,31,36,48]. Equation (23) also indicates the coefficient of the rotational coupling increases with $\frac{vb}{R^2}$ and would be dominant at small R , while radial coupling depends on v_R . Physically, one can think that the interaction time is long with slow collision energies, and the electronic cloud can be adapted to the smaller internuclear separation. This results in the larger populations of the $5p_1$ state through the rotational coupling. The interaction time will decrease with increasing the collision energy, and the population of the $5p_0$ state will increase. The DSADs of the sum of $5p_0$ and $5p_1$ states have resemblances between the TC-AOCC calculations and the experimentally obtained $1s \rightarrow 5p$ transition [cf. Figs. 4(e) and 4(h)]. This also implies the magnetic

quantum number information is well preserved in the $1s \rightarrow 5p_0$ and $1s \rightarrow 5p_1$ transitions. However, the single-center and single-active electron approximations of the H_2 molecules for the TC-AOCC calculation overestimate the yield of the first oscillatory lobe for $1s \rightarrow 5p_1$ transition and the larger DSADs for both $1s \rightarrow 5p_0$ and $1s \rightarrow 5p_1$ transitions. Similar behavior has been observed in the $1s \rightarrow 4p_0$ and $1s \rightarrow 4p_1$ transitions for the single-active electron approximation of the Ar^{8+} -He collision system [25,27].

2. Matter-wave diffraction

To understand the undulations in the small scattering angles, we present further analysis based on Fraunhofer-type diffraction in this section. The similarities between the Fraunhofer diffraction of light by a circular aperture and the electron transfer process for ion-atom collision are well known [18,47]. In the optical Fraunhofer diffraction theory, the intensity is given by [49]

$$I(\theta) \propto \left| \int_0^\rho r dr J_0(kr \sin \theta) f(r) \right|^2, \quad (25)$$

where r is the aperture radius, J_0 represents the Bessel function, k is the wave vector, θ is the diffraction angle, and $f(r)$ is the pupil function which reflects the radial transmittance and phase shift of the aperture. For a uniformly illuminated circular aperture, the above equation reduces to

$$I(\theta) \propto \left[\frac{2J_1(k\rho \sin \theta)}{k\rho \sin \theta} \right]^2. \quad (26)$$

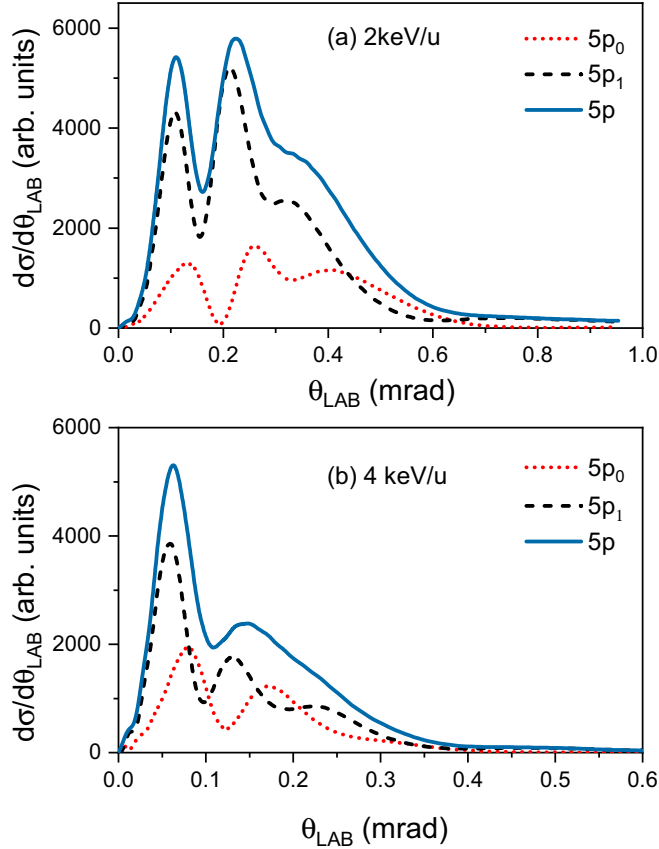


FIG. 5. DSADs of the state-selective electron capture for the $1s$ to $5s_0$ and $5p_1$ states are represented for the (a) 2 and (b) 4 keV/u Ar^{8+} - H_2 collisions. The dotted and dashed lines represent the $5p_0$ and $5p_1$ states, respectively, and are theoretically calculated using the TC-AOCC method. The blue line is the sum of $5p_0$ and $5p_1$ contributions.

The corresponding dark and bright diffraction fringes are given by $\sim 0.61\lambda/\rho$, $\sim 0.819\lambda/\rho$, $\sim 1.116\lambda/\rho$, etc., where λ is the wavelength of the incoming wave.

Analogous to optical diffraction [cf. Eq. (25)], the differential cross sections (DCSs) for $\Delta m_{fi} = 0$ transitions are given by the eikonal approximation [30,50],

$$\frac{d\sigma}{d\Omega} \propto \left| \int_0^b b db J_0(kb \sin \theta) g(b) \right|^2, \quad (27)$$

where θ is the scattering angle; $g(b)$ is the transmittance function for the electron capture process, including the internuclear interaction; b is the impact parameter, and $k = 2\pi/\lambda_{\text{dB}}$, with λ_{dB} being the de Broglie wavelength of the incoming projectile.

In the following, we use the reduced probability $bP(b)$, where $P(b) = |a_{fi}|^2$ of the electron capture (cf. Fig. 6 left panels), as guidance for estimating the radius of the collision region. Our Fraunhofer diffraction theory (FDT) model results are shown in Fig. 6 with the TC-AOCC calculations.

The $bP(b)$ distributions are pronounced in a definite range of impact parameters b . Therefore, one can assume the aperture functions are annular in nature rather than circular. In the case of a uniformly illuminated annular aperture of radii ϵa

TABLE II. Relative populations of the $5p_0$ and $5p_1$ states at 2 and 4 keV/u collision energies.

E (keV/u)	$5p_0$	$5p_1$
2	29.1	70.9
4	37.8	62.2

and a , the intensity distribution is given by [49]

$$I(\theta) \propto \frac{1}{(1 - \epsilon^2)^2} \left[\frac{2J_1(ka \sin \theta)}{ka \sin \theta} - \epsilon^2 \frac{2J_1(k\epsilon a \sin \theta)}{k\epsilon a \sin \theta} \right]^2, \quad (28)$$

where the value of ϵ is less than unity. For $\epsilon \rightarrow 0$, Eq. (28) gives the intensity distribution for a circular aperture. Figure 6 shows the reduced probability $bP(b)$ and the corresponding DSADs for the $1s \rightarrow 5s$ transition at 1, 2, and 4 keV/u collision energies. From the $bP(b)$ distributions [Figs. 6(a)–6(c)], one can observe that the probability of the electron capture is almost negligible in the smaller impact parameters b . Therefore, we have used the simple FDT model based on the uniformly illuminated annular aperture function. Our FDT model reproduced the position of the dark and bright fringes with the theoretically calculated DSADs based on the TC-AOCC model. We have tabulated the positions of the diffraction fringes obtained from the TC-AOCC method and the annular FDT model in Table III. The positions of the dark and bright fringes show an excellent agreement between the TC-AOCC calculation and the FDT model. The maximum of the $bP(b)$ extends to ~ 8.0 a.u. and results in the diffraction fringes in the much smaller scattering angles, which are proportional to $\sim \lambda_{\text{dB}}/b$. For 1, 2, and 4 keV/u collision energies the λ_{dB} values are $\sim 4.27 \times 10^{-4}$, 3.02×10^{-4} , and 2.14×10^{-4} a.u., respectively. Therefore, it is difficult to see these undulations (e.g., ≤ 0.07 mrad for 1 keV/u) in the experimental data as they also ride over the leading edge of the smooth Gaussian-like distributions. Classically, the

TABLE III. Positions of the diffraction fringes for the TC-AOCC theory are deduced for $1s$ - $5s$ SC processes. The diffraction patterns for a uniform annular aperture (ρ_a) predicted by the respective FDT model are also tabulated.

Energy (keV/u)	Diffraction fringes	TC-AOCC (mrad)	FDT annular (mrad)
1	1st dark	0.032	0.032
	1st bright	—	0.046
	2nd dark	0.067	0.068
2	1st dark	0.017	0.017
	1st bright	—	0.027
	2nd dark	0.039	0.039
4	1st dark	0.012	0.012
	1st bright	—	0.019
	2nd dark	0.028	0.028

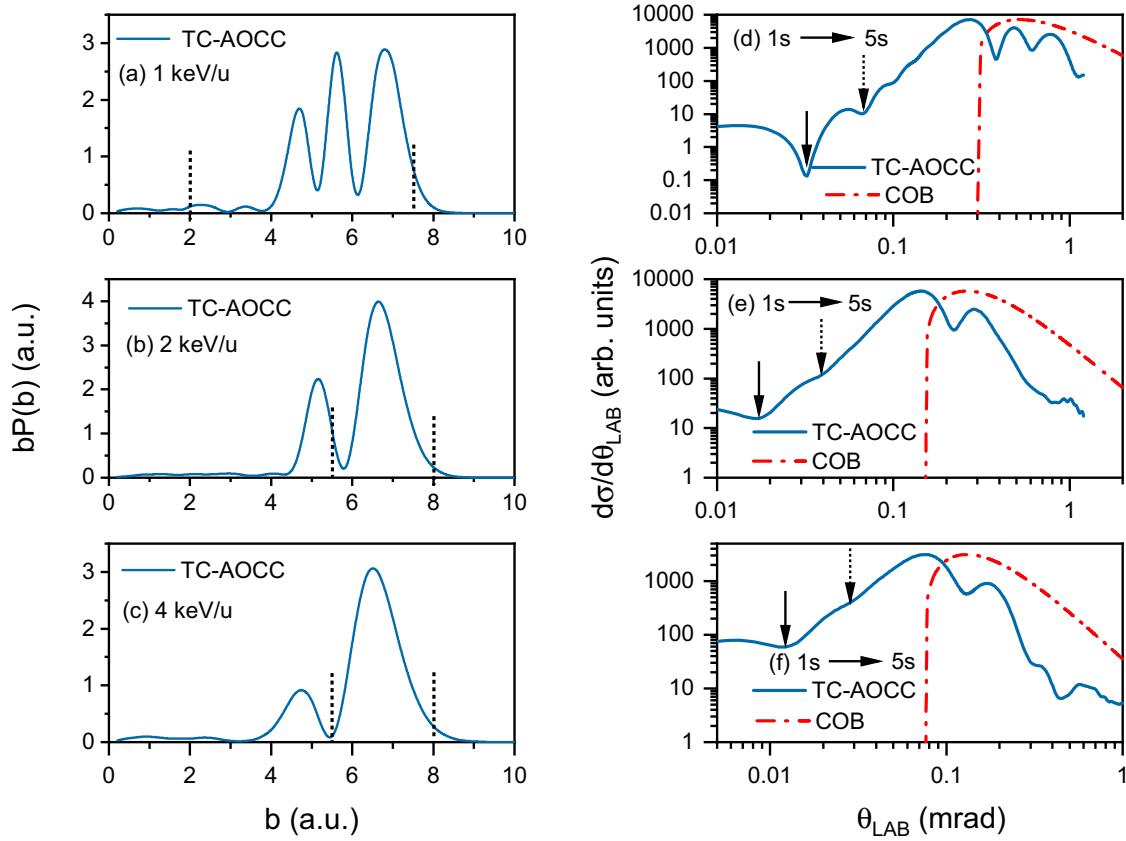


FIG. 6. The reduced probability $bP(b)$ (left panels) and the corresponding DSADs for the $1s$ to $5s$ states (right panels) are represented for the 1, 2, and 4 keV/u Ar^{8+} - H_2 collisions. The $bP(b)$ and the corresponding DSADs are calculated using the TC-AOCC method. The vertical black dotted lines indicate the range of the uniform annular apertures in panels (a), (b), and (c). Panels (d), (e), and (f) are plotted in the logarithmic scale to make the smaller scattering angles' undulations visible. The red dash-dotted lines (right panels) represent the DSADs, which are calculated from the COB model. The classical DSADs are normalized with the TC-AOCC calculations.

oscillations of the scattering-angle distributions correspond to the oscillations in the $bP(b)$ distributions. For example, at the 1 keV/u collision energy, the $bP(b)$ distribution has three oscillations between 4 and 8 a.u. impact parameters b and the DSADs have three oscillations above the scattering angles of ~ 0.2 mrad. The distant collisions or the higher impact parameters b result in the smaller scattering angles and vice versa. The oscillations in the DSADs come from the different impact parameters b , leading to similar scattering angles that might interfere constructively or destructively, leading to coherent oscillations. These oscillations are known as Stueckelberg-type oscillations and are mostly observed in slow collisions. Similar correspondence has been observed for the 2 and 4 keV/u $1s \rightarrow 5s$ transitions.

One can say that these Stueckelberg-type oscillations are the dominant contributions in the slow HCI-atom and -molecule collisions over the Fraunhofer diffraction-type structures. This can be understood as follows: In the intermediate- and high-energy collisions where the quasimolecular effect is less, the diffractionlike structures are mostly governed by the Coulomb repulsion between the target core and the projectile core, included in the eikonal phase [51]. For the intermediate- and high-energy He^{2+} -He and H^+ -He collisions [34,35], the transition amplitude a_{fi} is almost constant over the impact parameter b , and the eikonal phase $e^{2(i/v)Z_p Z_t \ln b}$ has a smooth

behavior as v is much higher and Z_p is smaller. This results in the dominant Fraunhofer diffractionlike structures. However, in the slow HCI-molecule collisions, the a_{fi} itself oscillates, and the eikonal phase also oscillates rapidly due to the high Z_p and smaller v . It can be seen that electronic dynamics in the quasimolecular region are governed by the molecular mechanisms that occur in the small internuclear separation through the curve crossing between the molecular states. These small- b -induced collisions result in the large scattering angles in the DSADs. On the other hand, diffractionlike structures arise from the large- b -induced collisions, i.e., soft collisions [47]. In these slow HCI-atom and -molecule collisions, molecular mechanisms dominantly govern electronic dynamics. Therefore, it results in the much shallower contribution of the Fraunhofer diffraction-type patterns and is mostly dominated by the Stueckelberg-type oscillations.

In the TC-AOCC calculations, the electronic motion is considered quantum mechanically, and transition amplitudes reflect the nature of the electronic transitions. The oscillations in the state-selective DSADs are quantum in nature, manifesting the Stueckelberg-type oscillations in the large scattering angles and the quantum matter-wave diffraction in the small scattering angles.

In order to validate the quantum oscillations in the angular distributions, we have calculated the classical DSADs

using the COB model [21,22]. Within the COB model, the transverse momentum arises from the Coulomb interaction between the two charged particles Z_P and Z_T , separated by R distance. If the projectile moves in the x direction, the perpendicular force component will give rise to the transverse momentum,

$$F_{\perp} = \frac{Z_P Z_T b}{(x^2 + b^2)^{3/2}}. \quad (29)$$

For a constant v , the transverse momentum ($p_{p\perp}$) along the projectile trajectory is

$$p_{p\perp} = \frac{1}{v} \int_{-\infty}^{\infty} F_{\perp} dx. \quad (30)$$

The $p_{p\perp}$ for m electrons capture as a function of b can be written as

$$p_{p\perp}(b) = \frac{1}{vb} \left[\sum_i^m \left(Z_P \sqrt{1 - \left(\frac{b}{R_i^{\text{in}}} \right)^2} + m \sqrt{1 - \left(\frac{b}{R_i^{\text{out}}} \right)^2} \right) + (Z_P - m)m \right], \quad (31)$$

where, for the single-electron capture process ($m = 1$), the capture radius during the way-in (R_i^{in}) and that during the way-out (R_i^{out}) of the collision are equal, i.e., $R_i^{\text{in}} = R_i^{\text{out}}$. Details of the calculation can be found elsewhere [52]. The differential cross section of the p_{\perp} distributions is obtained for the geometrical cross section $\sigma = \pi b^2$ as follows:

$$\frac{d\sigma}{dp_{p\perp}} = \frac{d\sigma}{db} \frac{db}{dp_{p\perp}} = 2\pi b \frac{db}{dp_{p\perp}}. \quad (32)$$

Using Eqs. (31) and (7), the above expression can be expressed in DSADs. The DSADs for $1s \rightarrow 5s$ transitions are calculated for $R_1^{\text{in}} = 8$ a.u. The red dash-dotted lines in Fig. 6 represent the DSADs calculated using the COB model. It can be clearly seen that the classical DSADs are Gaussian-like in nature and do not reflect any oscillating structures. Therefore, it can be concluded that the oscillations in the DSADs, i.e., Stueckelberg-type oscillations, and matter-wave diffraction are quantum in nature.

V. CONCLUSIONS

In conclusion, we have comprehensively studied the state-selective electron capture dynamics in the slow Ar^{8+} - H_2 collisions. The recoil ions and the charge-changing projectiles are coincidentally measured by combining the cold target recoil ion momentum spectrometer with the projectile final charge state analyzer. Using kinematics, the different state-selective projectile final states and scattering-angle distributions are obtained from the recoil longitudinal and transverse momentum transfers.

In our measured Q -value spectra, the relative populations of the state-selective single-electron capture from $1s$ to the highly excited $4d + 4f$, $5s$, $5p$, $5d + 5f + 5g$, $6s + 6p$, and $6d + 6f + 6g + 6h$ transitions are measured experimentally at 1, 2, and 4 keV/u collision energies. The differential-scattering-angle distributions for the dominant $1s$ to $5s$, $5p$, and $5d + 5f + 5g$ transitions are compared with the DSADs obtained from the TC-AOCC method. The oscillations in the DSADs are mostly reproduced by the TC-AOCC method except for a small shift in the scattering angles, which is mostly caused by the exclusion of the e - e correlation effect in the interaction potential. The relative populations of the $5p_0$ and $5p_1$ states show a collision-energy-dependence alignment of the electron's orbitals. The Stueckelberg-type of oscillations originates from the coherent superposition of the different impact parameters and is governed by the small- b -induced collisions. The shallow undulations in the smaller scattering angles mostly arise from the quantum matter-wave scatterings and are sensitive to collision energy. A mathematical model based on the optical Fraunhofer diffraction theory reproduced the positions of the dark and bright fringes for a uniformly illuminated annular aperture function. The quantum nature of the oscillating structures in the state-selective DSADs is further validated by classical calculations based on the COB model. Our studies provide insight into the different types of quantum scattering processes responsible for the oscillatory patterns in the small and large scattering angles for the highly excited quantum state-selective electron capture process.

ACKNOWLEDGMENTS

The authors wish to thank all the members of ECRIA for their help during the experiment. The authors also thank Dr. Hicham Agueny from the University of Bergen, Norway, for fruitful discussions about the collision dynamics. This work is supported by the Department of Atomic Energy (Government of India) research project RTI 4002.

- [1] M. A. Abdallah, W. Wolff, H. E. Wolf, E. Y. Kamber, M. Stöckli, and C. L. Cocke, Single and double electron capture from He by Ar^{16+} studied using cold-target recoil-ion momentum spectroscopy, *Phys. Rev. A* **58**, 2911 (1998).
- [2] N. Neumann, D. Hant, L. P. H. Schmidt, J. Titze, T. Jahnke, A. Czasch, M. S. Schöffler, K. Kreidi, O. Jagutzki, H. Schmidt-Böcking, and R. Dörner, Fragmentation dynamics of CO_2^{3+} investigated by multiple electron capture in collisions with slow highly charged ions, *Phys. Rev. Lett.* **104**, 103201 (2010).

- [3] J. Matsumoto, A. Leredde, X. Flechard, K. Hayakawa, H. Shiromaru, J. Rangama, C. L. Zhou, S. Guillous, D. Hennecart, T. Muranaka, A. Mery, B. Gervais, and A. Cassimi, Asymmetry in multiple-electron capture revealed by radiative charge transfer in Ar dimers, *Phys. Rev. Lett.* **105**, 263202 (2010).
- [4] X. Ma, S. Zhang, W. Wen, Z. Huang, Z. Hu, D. Guo, J. Gao, B. Najjari, S. Xu, S. Yan, K. Yao, R. Zhang, Y. Gao, and X. Zhu, Atomic structure and collision dynamics with highly charged ions, *Chin. Phys. B* **31**, 093401 (2022).

- [5] W. Wu, J. P. Giese, I. Ben-Itzhak, C. L. Cocke, P. Richard, M. Stockli, R. Ali, H. Schöne, and R. E. Olson, Velocity dependence of one- and two-electron processes in intermediate-velocity $\text{Ar}^{16+} + \text{He}$ collisions, *Phys. Rev. A* **48**, 3617 (1993).
- [6] B. H. Bransden and M. R. C. McDowell, *Charge Exchange and the Theory of Ion-Atom Collisions* (Oxford University, New York, 1992).
- [7] J. Ullrich and V. Shevelko, *Charge Exchange and the Theory of Ion-Atom Collisions* (Oxford University, New York, 1992).
- [8] N. Sisourat, I. Pilskog, and A. Dubois, Nonperturbative treatment of multielectron processes in ion-molecule scattering: Application to $\text{He}^{2+}\text{-H}_2$ collisions, *Phys. Rev. A* **84**, 052722 (2011).
- [9] P. Beiersdorfer, K. R. Boyce, G. V. Brown, H. Chen, S. M. Kahn, R. L. Kelley, M. May, R. E. Olson, F. S. Porter, C. K. Stahle, and W. A. Tillotson, Laboratory simulation of charge exchange-produced X-ray emission from comets, *Science* **300**, 1558 (2003).
- [10] J. E. Rice, E. S. Marmor, J. L. Terry, E. Kallne, and J. Kallne, Observation of charge-transfer population of high- n levels in Ar^{16+} from neutral hydrogen in the ground and excited states in a tokamak plasma, *Phys. Rev. Lett.* **56**, 50 (1986).
- [11] T. E. Cravens, X-ray emission from comets, *Science* **296**, 1042 (2002).
- [12] S. Uehara and H. Nikjoo, Monte Carlo track structure code for low-energy alpha-particles in water, *J. Phys. Chem. B* **106**, 11051 (2002).
- [13] R. Dörner, V. Mergel, O. Jagutzki, L. Spielberger, J. Ullrich, R. Moshhammer, and H. Schmidt-Böcking, Cold target recoil ion momentum spectroscopy: a ‘momentum microscope’ to view atomic collision dynamics, *Phys. Rep.* **330**, 95 (2000).
- [14] J. Ullrich, R. Moshhammer, A. Dorn, R. Dörner, L. P. H. Schmidt, and H. Schmidt-Böcking, Recoil-ion and electron momentum spectroscopy: reaction-microscopes, *Rep. Prog. Phys.* **66**, 1463 (2003).
- [15] NIST: Atomic Spectra Database, Energy Levels, https://physics.nist.gov/PhysRefData/ASD/levels_form.html.
- [16] M. A. Abdallah, W. Wolff, H. E. Wolf, E. Sidky, E. Y. Kamber, M. Stöckli, C. D. Lin, and C. L. Cocke, Cold-target recoil-ion-momentum spectroscopy study of single electron capture from He by slow Ar^{8+} ions, *Phys. Rev. A* **57**, 4373 (1998).
- [17] M. van der Poel, C. V. Nielsen, M.-A. Gearba, and N. Andersen, Fraunhofer diffraction of atomic matter waves: Electron transfer studies with a laser cooled target, *Phys. Rev. Lett.* **87**, 123201 (2001).
- [18] M. van der Poel, C. V. Nielsen, M. Rybaltov, S. E. Nielsen, M. Machholm, and N. Andersen, Atomic scattering in the diffraction limit: electron transfer in keV $\text{Li}^+\text{-Na}(3s, 3p)$ collisions, *J. Phys. B: At., Mol. Opt. Phys.* **35**, 4491 (2002).
- [19] A. Leredde, A. Cassimi, X. Fléchar, D. Hennecart, H. Jouin, and B. Pons, Atomic-matter-wave diffraction evidenced in low-energy $\text{Na}^+ + \text{Rb}$ charge-exchange collisions, *Phys. Rev. A* **85**, 032710 (2012).
- [20] S. Otranto, I. Blank, R. E. Olson, and R. Hoekstra, Evidence of electron saddle swap oscillations in angular differential ion-atom charge exchange cross sections, *J. Phys. B: At., Mol. Opt. Phys.* **45**, 175201 (2012).
- [21] H. Ryufuku, K. Sasaki, and T. Watanabe, Oscillatory behavior of charge transfer cross sections as a function of the charge of projectiles in low-energy collisions, *Phys. Rev. A* **21**, 745 (1980).
- [22] A. Niehaus, A classical model for multiple-electron capture in slow collisions of highly charged ions with atoms, *J. Phys. B: At., Mol. Opt. Phys.* **19**, 2925 (1986).
- [23] M. Druetta, S. Martin, T. Bouchama, C. Harel, and H. Jouin, Spectroscopic study of the charge-exchange collision between Ar^{8+} and He or H_2 at beam energies of 80, 40, and 8 keV, *Phys. Rev. A* **36**, 3071 (1987).
- [24] M. Alessi, N. D. Cariatore, P. Focke, and S. Otranto, State-selective electron capture in $\text{He}^+ + \text{H}_2$ collisions at intermediate impact energies, *Phys. Rev. A* **85**, 042704 (2012).
- [25] R. T. Zhang, X. L. Zhu, X. Y. Li, L. Liu, S. F. Zhang, W. T. Feng, D. L. Guo, Y. Gao, D. M. Zhao, J. G. Wang, and X. Ma, Single-electron capture in 3-keV/u $\text{Ar}^{8+}\text{-He}$ collisions, *Phys. Rev. A* **95**, 042702 (2017).
- [26] M. A. K. A. Siddiki, M. Nrishimhamurty, K. Kumar, J. Mukherjee, L. C. Tribedi, A. Khan, and D. Misra, Development of a cold target recoil ion momentum spectrometer and a projectile charge state analyzer setup to study electron transfer processes in highly charged ion-atom/molecule collisions, *Rev. Sci. Instrum.* **93**, 113313 (2022).
- [27] R. T. Zhang, J. W. Gao, Y. W. Zhang, D. L. Guo, Y. Gao, X. L. Zhu, J. W. Xu, D. M. Zhao, S. Yan, S. Xu, S. F. Zhang, Y. Wu, J. G. Wang, and X. Ma, Strongly perturbed state-selective charge exchange between slow Ar^{8+} and He, *Phys. Rev. Res.* **5**, 023123 (2023).
- [28] W. Fritsch and C. Lin, The semiclassical close-coupling description of atomic collisions: Recent developments and results, *Phys. Rep.* **202**, 1 (1991).
- [29] Y. W. Zhang, J. W. Gao, Y. Wu, J. G. Wang, N. Sisourat, and A. Dubois, Single- and double-electron capture in intermediate-energy $\text{Ar}^{8+} + \text{He}$ collisions, *Phys. Rev. A* **106**, 042809 (2022).
- [30] A. Dubois, S. E. Nielsen, and J. P. Hansen, State selectivity in $\text{H}^+\text{-Na}(3s/3p)$ collisions: differential cross sections, alignment and orientation effects for electron capture, *J. Phys. B: At., Mol. Opt. Phys.* **26**, 705 (1993).
- [31] T. G. Winter, G. J. Hatton, and N. F. Lane, Molecular-state treatment of collisions between protons and He^+ ions, *Phys. Rev. A* **22**, 930 (1980).
- [32] W. Fritsch, Theoretical study of electron processes in slow $\text{He}^{2+}\text{-He}$ collisions, *J. Phys. B: At., Mol. Opt. Phys.* **27**, 3461 (1994).
- [33] M. A. K. A. Siddiki, J. Mukherjee, K. Kumar, K. Tórkési, D. Misra, and H. Agueny, Observing quantum matter-wave diffraction in the energetic $\text{He}^{2+}\text{-He}$ collisions, *Phys. Rev. Res.* **6**, 013108 (2024).
- [34] H. Agueny, Fraunhofer-type diffraction patterns of matter-wave scattering of projectiles: Electron transfer in energetic ion-atom collisions, *Phys. Rev. A* **92**, 012702 (2015).
- [35] M. Gudmundsson, D. Fischer, N. Haag, H. A. B. Johansson, D. Misra, P. Reinhard, H. Schmidt-Böcking, R. Schuch, M. Schöffler, K. Stöckel, H. T. Schmidt, and H. Cederquist, Angular scattering in fast ion-atom electron transfer collisions: projectile wave diffraction and Thomas mechanisms, *J. Phys. B: At., Mol. Opt. Phys.* **43**, 185209 (2010).
- [36] C. H. Liu, J. G. Wang, and R. K. Janev, Single- and double-charge transfer in slow $\text{He}^{2+}\text{-He}$ collisions, *J. Phys. B: At., Mol. Opt. Phys.* **45**, 235203 (2012).

- [37] E. C. G. Stückelberg, Theory of inelastic collisions between atoms, *Helv. Phys. Acta (Basel)* **5**, 369 (1932).
- [38] A. Barany, H. Danared, H. Cederquist, P. Hvelplund, H. Knudsen, J. O. K. Pedersen, C. L. Cocke, L. N. Tunnell, W. Waggoner, and J. P. Giese, Stueckelberg angular scattering oscillations in two-electron capture by C^{4+} from He at low energies, *J. Phys. B: At., Mol. Opt. Phys.* **19**, L427 (1986).
- [39] R. E. Olson and F. T. Smith, Collision spectroscopy. IV. Semi-classical theory of inelastic scattering with applications to $He^+ + Ne$, *Phys. Rev. A* **3**, 1607 (1971).
- [40] L. Liu, C. H. Liu, J. G. Wang, and R. K. Janev, Cross sections for electron capture in $H^+ - Li(2p\sigma, \pi^\pm)$ collisions, *Phys. Rev. A* **84**, 032710 (2011).
- [41] A. N. Agnihotri, A. H. Kelkar, S. Kasthurirangan, K. V. Thulasiram, C. A. Desai, W. A. Fernandez, and L. C. Tribedi, An ECR ion source-based low-energy ion accelerator: development and performance, *Phys. Scr.* **2011**, 014038 (2011).
- [42] M. A. K. A. Siddiki, L. C. Tribedi, and D. Misra, Probing the fragmentation pathways of an argon dimer in slow ion-dimer collisions, *Atoms* **11**, 34 (2023).
- [43] W. C. Wiley and I. H. McLaren, Time-of-flight mass spectrometer with improved resolution, *Rev. Sci. Instrum.* **26**, 1150 (1955).
- [44] A. Khan, L. C. Tribedi, and D. Misra, A recoil ion momentum spectrometer for molecular and atomic fragmentation studies, *Rev. Sci. Instrum.* **86**, 043105 (2015).
- [45] P. Boduch, M. Chantepie, D. Hennecart, X. Husson, H. Kucal, D. Lecler, N. Stolterfoht, M. Druetta, B. Fawcett, and M. Wilson, Spectroscopic analysis of visible and near UV light emitted by Ar^{7+} and Ar^{6+} ions produced in $Ar^{8+} - He$ and $Ar^{8+} - H_2$ collisions at 120 keV, *Phys. Scr.* **45**, 203 (1992).
- [46] A. Kumar and B. C. Saha, State-selective charge transfer in slow collisions of partially stripped He-like ions with H_2 , *Phys. Rev. A* **59**, 1273 (1999).
- [47] D. L. Guo, J. W. Gao, S. F. Zhang, X. L. Zhu, Y. Gao, D. M. Zhao, R. T. Zhang, Y. Wu, J. G. Wang, A. Dubois, and X. Ma, State-selective single-electron capture in intermediate-energy $C^{4+} + He$ collisions, *Phys. Rev. A* **103**, 032827 (2021).
- [48] N. Andersen, J. T. Broad, E. E. Campbell, J. W. Gallagher, and I. V. Hertel, Collisional alignment and orientation of atomic outer shells. II. Quasi-molecular excitation, and beyond, *Phys. Rep.* **278**, 107 (1997).
- [49] M. Born and E. Wolf, *Principles of Optics: Electromagnetic Theory of Propagation, Interference, and Diffraction of Light* (Elsevier, 2013).
- [50] L. Wilets and S. J. Wallace, Eikonal method in atomic collisions. I, *Phys. Rev.* **169**, 84 (1968).
- [51] H. Agueny, étude théorique des processus électroniques ayant lieu au cours de collisions atomiques et moléculaires: approches non perturbatives, Ph.D. thesis, Université Paris-Sorbonne, Paris IV, 2014.
- [52] S. Knoop, Electron dynamics in ion-atom interactions, Ph.D. thesis, University of Groningen, 2006.